Inorganic Chemistry

Article

pubs.acs.org/IC

Study on the Reversible Electrode Reaction of $Na_{1-x}Ni_{0.5}Mn_{0.5}O_2$ for a Rechargeable Sodium-Ion Battery

Shinichi Komaba,* Naoaki Yabuuchi, Tetsuri Nakayama, Atsushi Ogata, Toru Ishikawa, and Izumi Nakai

Department of Applied Chemistry, Tokyo University of Science, 1-3 Kagurazaka, Shinjuku, Tokyo 162-8601, Japan

Supporting Information

ABSTRACT: Layered $NaNi_{0.5}Mn_{0.5}O_2$ (space group: $R\bar{3}m$), having an O3-type (α-$NaFeO_2$ type) structure according to the Delmas' notation, is prepared by a solid-state method. The electrochemical reactivity of $NaNi_{0.5}Mn_{0.5}O_2$ is examined in an aprotic sodium cell at room temperature. The $NaNi_{0.5}Mn_{0.5}O_2$ electrodes can deliver ca. 105−125 mAh g^{-1} at rates of 240−4.8 mA g^{-1} in the voltage range of 2.2−3.8 V and show 75% of the initial reversible capacity after 50 charge/discharge cycling tests. In the voltage range of 2.2−4.5 V, a higher reversible capacity of 185 mAh g^{-1} is achieved; however, its reversibility is insufficient because of the significant expansion of interslab space by charging to 4.5 V versus sodium. The reversbility is improved by adding fluoroethylene carbonate into the electrolyte solution. The structural transition mechanism of $Na_{1-x}Ni_{0.5}Mn_{0.5}O_2$ is also examined by an ex situ X-ray diffraction method combined with X-ray absorption spectroscopy (XAS). The staking sequence of the $[Ni_{0.5}Mn_{0.5}]O_2$ slabs changes progressively as sodium ions are extracted from the crystal lattice. It is observed that the original O3 phase transforms into the O′3, P3, P′3, and P3″ phases during sodium extraction. XAS measurement proves that $NaNi_{0.5}Mn_{0.5}O_2$ consists of divalent nickel and tetravalent manganese ions. As sodium ions are extracted from the oxide to form $Na_{1-x}Ni_{0.5}Mn_{0.5}O_2$, nickel ions are oxidized to the trivalent state, while the manganese ions are electrochemically inactive as the tetravalent state.

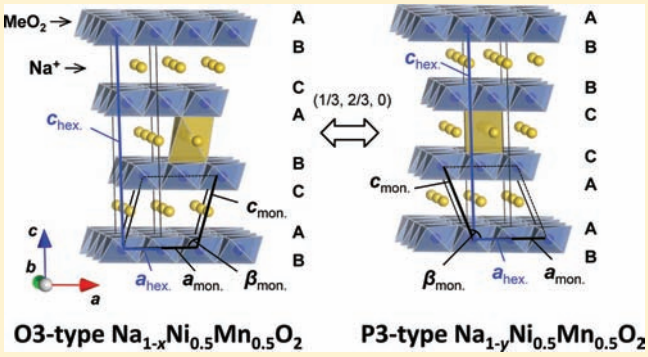

INTRODUCTION

Recently, the demands for an energy-efficient transportation system are rapidly growing in the world. Electric vehicles are being developed for commercial use, which are equipped with largely packed rechargeable lithium-ion batteries. Because the application area of the lithium-ion batteries has been expanded, lithium mining and production have been significantly increased in the past decade. Its production will be further increased with the growing market of electric vehicles, inevitably resulting in increasing cost of the lithium resources. If the sodium insertion materials are substitutable for lithium insertion materials in lithium-ion batteries, there will appear to be a significant advantage of a natural abundance of sodium because of the lithium-free battery system, i.e., a rechargeable sodium-ion battery. Although many sodium transition-metal oxides are known to be electrochemically active accompanied by sodium extraction/insertion, a limited number of successful reports showing a highly reversible capacity with satisfactory retention for battery application are found, compared to the extensively studied lithium system.

In the 1970−1980s, layered transition-metal dichalcogenides were examined in aprotic sodium cells. A list of the (di)chalcogenide materials examined as sodium insertion hosts is found in a review paper written by Abraham.[1] Layered transition-metal oxides, $NaMeO_2$ (Me = transition metal), have also been examined in the sodium cells, e.g., Na_xCoO_2,[2] $NaNi_{0.6}Co_{0.4}O_2$,[3] Na_xMnO_2,[4] $NaNi_{0.5}Fe_{0.5}O_2$,[5] $NaNi_{0.5}Ti_{0.5}O_2$,[5] and $NaFeO_2$.[5,6] In addition to the layered oxide system, several materials have been reported as sodium insertion hosts so far, such as WO_3,[7] spinel-type oxides (Fe_3O_4, etc.[8]), distorted MoO_3-type iron fluoride (FeF_3[9]), iron phosphates,[10] Na_2FePO_4F,[11] etc. To our knowledge, the highest reversible capacity with a high operating voltage (>2.5 V) such as the positive electrode materials is reported by using sodium−nickel−manganese oxides, i.e., P2-type $Na_{2/3}Ni_{1/3}Mn_{2/3}O_2$ by Lu and Dahn's group.[12] They demonstrated more than 160 mAh g^{-1} reversible capacity for $Na_{2/3}Ni_{1/3}Mn_{2/3}O_2$ as the electrode materials. $Na_{2/3}Ni_{1/3}Mn_{2/3}O_2$ crystallizes into a layered structure, but the stacking sequences are different from those of conventional sodium layered materials such as $Na_{1.0}CoO_2$ having a cubic-close-packed (CCP) oxygen array. According to the structural classification of the layered oxides proposed by Delmas et al.,[13] $Na_{1.0}CoO_2$ and $Na_{2/3}Ni_{1/3}Mn_{2/3}O_2$ are categorized as O3 and P2 types, respectively. Generally, the cycleability of the sodium insertion host materials is worse than that of the lithium hosts, which is considered to be due to electrolyte decomposition at higher potential. Indeed, the lithium/(P2-type $Na_{2/3}CoO_2$) cell has retained 60−80% of the initial capacity after 300 cycling tests in

Received: February 17, 2012
Published: May 24, 2012

   dx.doi.org/10.1021/ic300357d | Inorg. Chem. 2012, 51, 6211−6220

the limited voltage range between 1.5 and 3.3 V.[2b] Johnson and co-workers reported P2-type $Na_{0.85}Li_{0.17}Ni_{0.21}Mn_{0.64}O_2$ as 3 V class positive electrode materials showing good reversibility.[14] Recently, we have reported that O3-type $NaCrO_2$ and $NaNi_{0.5}Mn_{0.5}O_2$ are electrochemically active, which can deliver more than 100 mAh g^{-1} of the reversible capacity after 50 continuous cycling tests.[15]

As the positive electrode material of rechargeable lithium-ion batteries, lithium−nickel−manganese oxide, $LiNi_{0.5}Mn_{0.5}O_2$, was extensively studied as the electrode material for rechargeable lithium-ion batteries.[16] The electrochemical reversibility of lithium extraction from $LiNi_{0.5}Mn_{0.5}O_2$ suffers from Ni^{2+} contamination in the Li^+ layer, resulting from cation intermixing between Li^+ and Ni^{2+} ions (~10%), which originates from the similarity of their ionic sizes (Li^+ = 0.76 Å; Ni^{2+} = 0.69 Å[17]). In contrast to $LiNi_{0.5}Mn_{0.5}O_2$, $NaNi_{0.5}Mn_{0.5}O_2$ having an ideal layered structure with no cation intermixing is reliably crystallized because the size of the sodium ion (1.02 Å[17]) is much larger than that of the lithium ion. Therefore, $NaNi_{0.5}Mn_{0.5}O_2$ has been used as the precursor to prepare $LiNi_{0.5}Mn_{0.5}O_2$ with less intermixing by an ion-exchange method.[18] We recently succeeded in demonstrating the stable cycle performance for a 3 V rechargeable sodium-ion battery of hard carbon/$NaNi_{0.5}Mn_{0.5}O_2$ configuration.[15c] In this paper, we report the analysis of the electrode performance of $NaNi_{0.5}Mn_{0.5}O_2$ in the sodium cell. Its reaction mechanism is also examined by X-ray diffraction (XRD) and X-ray absorption spectroscopy (XAS). From these results, we will discuss the possibility of $NaNi_{0.5}Mn_{0.5}O_2$ as the positive electrode material for a rechargeable sodium-ion battery.

EXPERIMENTAL SECTION

The synthesis method of $NaNi_{0.5}Mn_{0.5}O_2$ can be found in the literature.[15b] $NaNi_{0.5}Mn_{0.5}O_2$ was prepared from a mixture of coprecipitated $Ni_{0.5}Mn_{0.5}(OH)_2$ and Na_2CO_3 powders (5% sodium excess based on the stoichiometric composition). The mixture of $Ni_{0.5}Mn_{0.5}(OH)_2$ and Na_2CO_3 was pelletized and then heat-treated at 800 °C in air for 24 h. The heated pellets were quenched to room temperature and stored in an argon-filled glovebox until use. The resultant product was handled in an inert atmosphere to avoid damage by moisture. The crystal structures of the samples were characterized by XRD (MultiFlex, Rigaku Corp., Ltd.) equipped with a graphite monochromator with Cu Kα radiation. XRD data of as-prepared $NaNi_{0.5}Mn_{0.5}O_2$ were analyzed by the Rietveld refinement program *RIETAN 2000*.[19]

A beaker-type cell was used to evaluate for the electrode performance in a sodium cell. Positive electrodes consisted of $NaNi_{0.5}Mn_{0.5}O_2$:acetylene black:PVdF = 8:1:1 (by weight). The electrode components were thoroughly mixed in *N*-methylpyrrolidone to form a uniform black slurry, and then the slurry was pasted to a stainless steel mesh current collector and dried in vacuum at 80 °C. A thin plate of sodium metal was used as negative electrodes. The electrolyte solution used was 1 mol dm^{-3} $NaClO_4$ dissolved in propylene carbonate (PC). Preparation of the electrodes and electrochemical cell was carefully carried out under highly dehydrated conditions in order to suppress deterioration by contamination.[15c] Electrochemical charge and discharge tests were carried out at room temperature (ca. 25 °C). The structural changes during the charge/discharge tests were examined by an ex situ XRD technique.

XAS was performed at the Beamline BL-12C of the Photon Factory Synchrotron Source at KEK, Japan. The spectra were collected with a silicon monochromator in transmission mode. The intensities of incident and transmitted X-rays were measured using an ionization chamber at room temperature. The samples were sealed in a water-resistant polymer film in an argon-filled glovebox. Analysis of the XAS spectra was carried out by using the program code of *IFEFFIT*.[20] The postedge background was determined using a cubic-spline procedure. The normalized extended X-ray absorption fine structure (EXAFS) spectra were converted from energy to wavevector k and then weighted by k^3. EXAFS structural parameters were obtained by a nonlinear least-squares analysis of the data using phase shift and amplitude function generated from the *FEFF* code.[21] The least-squares curve fitting was carried out in R space.

RESULTS AND DISCUSSION

Characterization of As-Prepared $NaNi_{0.5}Mn_{0.5}O_2$. The crystal structure and phase purity of O3-type $NaNi_{0.5}Mn_{0.5}O_2$ were examined by an XRD method. Figure 1 shows a XRD pattern of $NaNi_{0.5}Mn_{0.5}O_2$ and its refined results by the Rietveld method. All Bragg diffraction lines of the sample are assigned to rhombohedral symmetry with a space group $R\bar{3}m$, which is isostructural with α-$NaFeO_2$, and no crystalline impurity was observed in the diffratogram. From the structural refinement, unit cell parameters are calculated as a_{hex} = 2.9623(3) Å and c_{hex} = 15.955(2) Å in a hexagonal setting. These values are identical with those in a previous report.[18b] Rietveld analysis clearly demonstrated that intermixing between the sodium and nickel ions is negligible, as shown in Table 1.

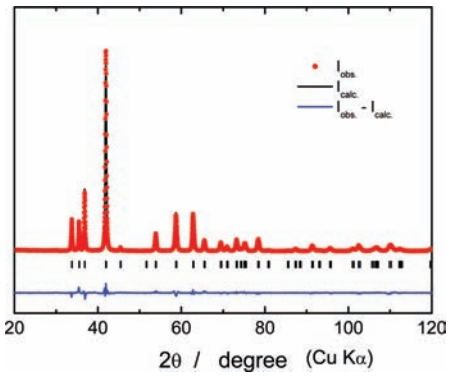

Figure 1. Results of the Rietveld refinement on a powder XRD pattern of $NaNi_{0.5}Mn_{0.5}O_2$. Structural parameters are listed in Table 1.

Table 1. Structural Parameters of $NaNi_{0.5}Mn_{0.5}O_2$ Refined by the Rietveld Method[a]

formula				$NaNi_{0.5}Mn_{0.5}O_2$		
space group				$R\bar{3}m$		
a_{hex} = 2.9623(3) Å, c_{hex} = 15.955(2) Å						
R_{wp} = 8.17%, R_I = 1.91%, S = 1.13						
atom	site	x	y	z	B (Å^2)	g^b
Na	3b	0	0	$^1/_2$	1.0[b]	1.0
Ni	3a	0	0	0	0.21(3)	0.5
Mn	3a	0	0	0	0.21(3)	0.5
O	6c	0	0	0.2678(3)	0.39(5)	1.0

[a]The isotropic displacement parameter (B) of the sodium (3b) site and occupation (g) of all sites were fixed. [b]Not refined.

Site occupation of nickel ions in the sodium layer (3b sites) was not assumed in the Rietveld analysis. Nevertheless, reliable parameters, which are the criteria for the fit, are reasonably small (R_{wp} = 8.17% and S = 1.13). Note that evidence of the in-plane long-range ordering of manganese and nickel, which was typically reported in $LiNi_{0.5}Mn_{0.5}O_2$ prepared by calcination of LiOH and $(Ni,Mn)(OH)_2$,[22] was not found in $NaNi_{0.5}Mn_{0.5}O_2$ not only by XRD but also by the electron diffraction method

dx.doi.org/10.1021/ic300357d | *Inorg. Chem.* 2012, 51, 6211−6220

(Figure S1 in the Supporting Information), which is in good agreement with the previous report by Kang et al.[18b] From these results, it is concluded that $NaNi_{0.5}Mn_{0.5}O_2$ crystallizes into an ideal O3-type layered structure without cation mixing defects and nickel/manganese in-plane ordering.

The morphology of $NaNi_{0.5}Mn_{0.5}O_2$ particles was observed by using scanning electron microscopy (SEM). Figure 2 shows

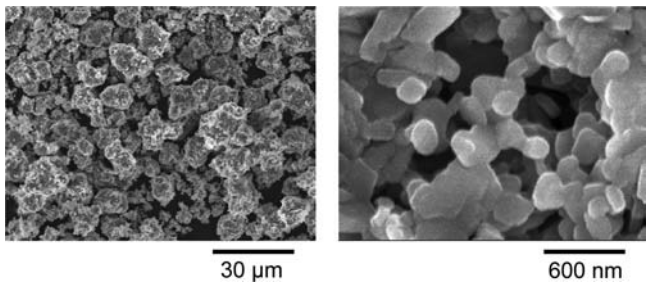

Figure 2. Morphology of as-prepared $NaNi_{0.5}Mn_{0.5}O_2$ observed by SEM.

SEM images of as-prepared $NaNi_{0.5}Mn_{0.5}O_2$, which were collected at different magnifications. Its primary particle size ranges from 100 to 500 nm, and the primary particles have polyhedral shape and could be single crystals. The particles agglomerate into larger secondary particles whose diameter was 10−20 μm. As a result, the highly crystalline $NaNi_{0.5}Mn_{0.5}O_2$ was synthesized by calcination of the mixture of precipitated $Ni_{0.5}Mn_{0.5}(OH)_2$ and Na_2CO_3 at 800 °C in air. The electrochemical insertion of sodium was further investigated in aprotic sodium cells.

Electrochemical Properties of $NaNi_{0.5}Mn_{0.5}O_2$ in Sodium Cells. Galvanostatic charge and discharge (oxidation and reduction, respectively) tests of sodium/$NaNi_{0.5}Mn_{0.5}O_2$ cells were carried out at room temperature (ca. 25 °C) using beaker-type cells, as shown in Figure 3. The sodium cell was

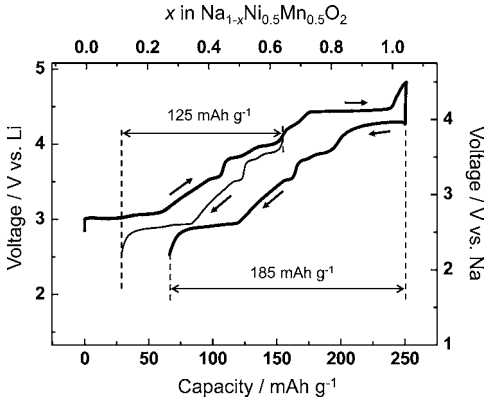

Figure 3. Initial charge and discharge curves of the sodium/$NaNi_{0.5}Mn_{0.5}O_2$ cell at a rate of 1/50 C (4.8 mA g^{-1}) in the voltage ranges of 2.2−3.8 and 2.2−4.5 V versus sodium metal. The voltage of the cell versus lithium is also shown for comparison.

charged to 3.8 or 4.5 V versus sodium and then discharged to 2.2 V versus sodium at a slower rate of 1/50 C (4.8 mA g^{-1}) to distinguish between one- and two-phase reactions, resulting in S-shaped and plateau curves, respectively. When the current passed is assumed to be consumed by sodium extraction from the oxide without any side reactions, almost all of the sodium ions are extracted from the crystal lattice of $NaNi_{0.5}Mn_{0.5}O_2$ by charging to 4.5 V, as seen in Figure 3. The first discharge capacity reaches 185 mAh g^{-1} under this experimental condition. To our knowledge, the observed reversible capacity of $NaNi_{0.5}Mn_{0.5}O_2$ above 2.2 V versus sodium is one of the highest values among the O3-type layered oxides tested in sodium cells reported in the literature so far, which is a level similar to that of the O3-type $NaMnO_2$ electrode.[4b]

A stepwise voltage profile is clearly noted during charge/discharge at a slow current rate. The voltage plateau seems to be reversible, although the irreversible capacity is included during the oxidation process because of the electrochemical decomposition of the electrolyte components.[23] The charge and discharge curves show reversible voltage variation, implying that the reversible structural transition process from the O3-type phase occurs during sodium extraction/insertion. The discharge capacity of 185 mAh g^{-1}, however, declines rapidly as a function of the cycling number, as shown in Figure 4. The reversible capacity of the beaker-type cells is reduced to less than 100 mAh g^{-1} after 10 cycles in the voltage range of 2.0−4.5 V at 1/30 C (Figure 4a). Polarization of the cell is also significantly increased. The capacity retention of Na/$NaNi_{0.5}Mn_{0.5}O_2$ cells is clearly influenced by the selection of the cutoff voltage upon charge.

While the discharge capacity is reduced to 125 mAh g^{-1} by restricting the voltage range of 2.2−3.8 V at 1/50 C rate, the capacity retention of the cell is drastically improved (Figure 4b); that is, more than 95% capacity of the initial value is retained after 10 cycles under this condition. The dependence of the current density on the discharge capacity is also examined. Figure 4c shows the first charge and discharge capacities of sodium/$NaNi_{0.5}Mn_{0.5}O_2$ cells at different current densities. The discharge capacity slightly decreases from 125 mAh g^{-1} at 1/30 C to 105 mAh g^{-1} at 1 C (240 mA g^{-1}), and polarization of the cells increases with the current density. Considering the previous data of the rate capability for layered lithium insertion materials, $NaNi_{0.5}Mn_{0.5}O_2$ electrodes demonstrate a satisfactory rate capability regardless of the relatively large particle size of about >10 μm, as described in Figure 2. The rate capability would be superior to that of layered lithium transition-metal oxides. It is thought that the diffusion of Na^+ ions is faster than that of Li^+ ions in the oxide framework because of a longer alkali−oxygen bonding, resulting in the weaker electrostatic interaction as we recently described for $NaCrO_2$[15a] and was supported by the first-principles calculation.[24] For O3-type layered oxides, such as $NaCoO_2$, the diffusion barriers for sodium in the host structures are lowered compared to those for the lithium system.[24] Additionally, it is generally known that solvation of the dissolved Na^+ ion is weaker than that of the Li^+ ion in the PC solution; therefore, the faster transport of Na^+ ions than Li^+ ions is expected in the PC solution.[15c] Consequently, the rate capability of $NaNi_{0.5}Mn_{0.5}O_2$ originates from the faster Na^+ transport in both the solid electrode and liquid electrolyte.

The capacity retention at different current densities was also examined with cutoff voltages of 2.2 and 3.8 V. The changes in the discharge capacity of the sodium cells during 50 cycles at 1/5 and 1 C rates are plotted in Figure 4d. Under both conditions, 75% of the capacity is retained after 50 charge/discharge cycling tests. Recently, we reported that capacity degradation was successfully suppressed by fluoroethylene carbonate (FEC) as the electrolyte additive in the PC electrolyte solution, resulting from suppression of the electrolyte decomposition at both $Na_xNi_{0.5}Mn_{0.5}O_2$ and sodium metal

dx.doi.org/10.1021/ic300357d | Inorg. Chem. 2012, 51, 6211−6220

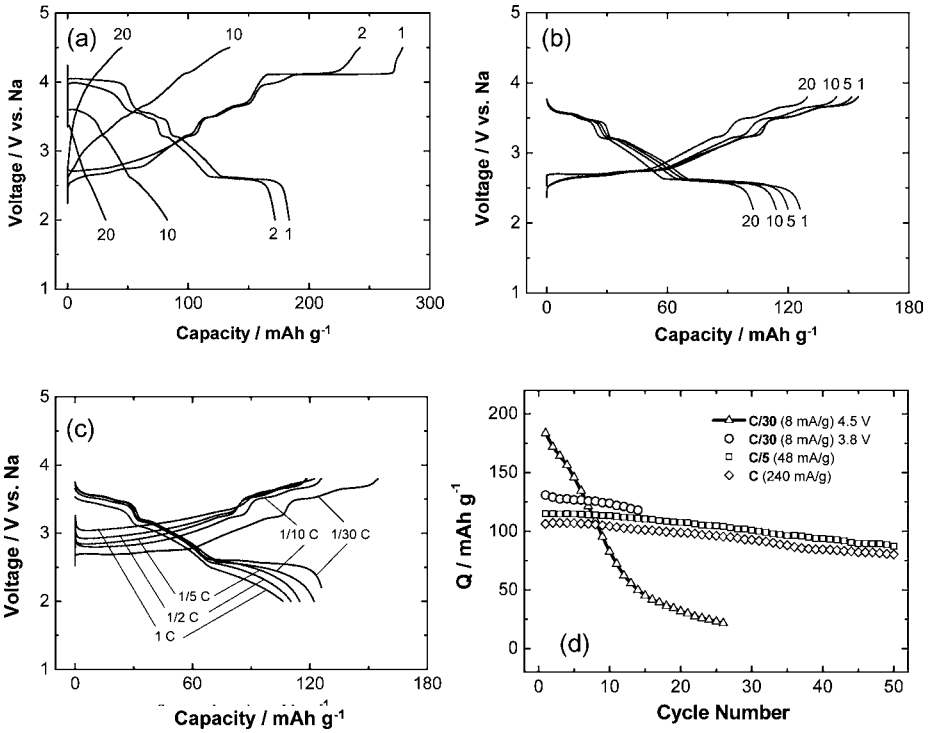

Figure 4. Galvanostatic charge/discharge curves of sodium/$NaNi_{0.5}Mn_{0.5}O_2$ beaker-type cells at a rate of 1/30 C (8 mA g^{-1}) in the voltage ranges of (a) 2.0−4.5 V and (b) 2.2−3.8 V. (c) First charge/discharge curves of sodium/$NaNi_{0.5}Mn_{0.5}O_2$ cells in the voltage range of 2.0−3.8 V at different rates: C/30 (8 mA g^{-1}), C/10 (24 mA g^{-1}), C/5 (48 mA g^{-1}), C/2 (120 mA g^{-1}), and 1C rate (240 mA g^{-1}). (d) Discharge capacity retention of sodium/$NaNi_{0.5}Mn_{0.5}O_2$ cells under different experimental conditions.

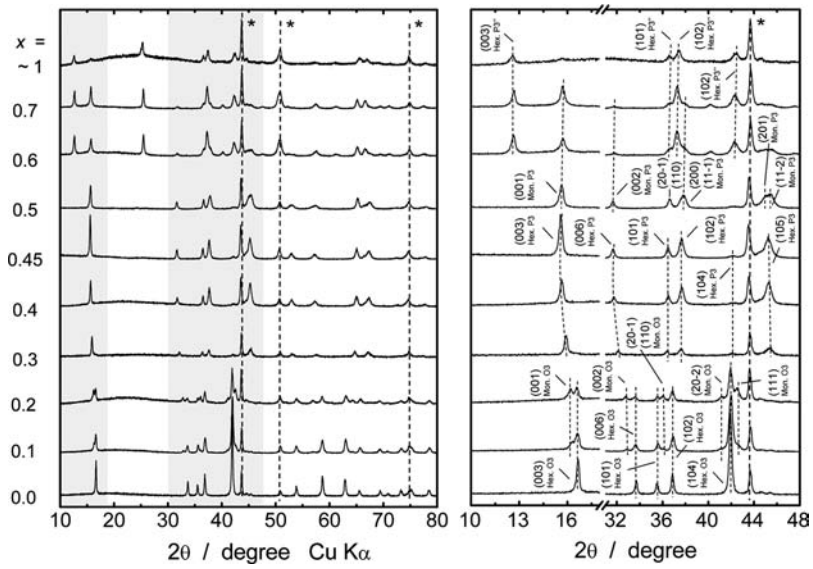

Figure 5. (Left) Ex situ XRD patterns of the $Na_{1-x}Ni_{0.5}Mn_{0.5}O_2$ composite electrodes on a nickel current collector, which were electrochemically prepared in the sodium cells. (Right) Highlighted XRD patterns. Asterisks show a nickel mesh used as a current collector.

electrodes.[23] The electrolyte additive highly improves the coulomb efficiency, indicating suppression of the oxidative decomposition.

Ex Situ XRD Study of $Na_{1-x}Ni_{0.5}Mn_{0.5}O_2$. To examine the reaction mechanism of $Na_{1-x}Ni_{0.5}Mn_{0.5}O_2$, the changes in the crystal structures were examined by an ex situ XRD method. Figure 5 shows the ex situ XRD patterns of the $Na_{1-x}Ni_{0.5}Mn_{0.5}O_2$ composite electrodes. The electrode samples were prepared in the sodium cells by applying a constant oxidation current to $NaNi_{0.5}Mn_{0.5}O_2$ for a given duration to fix the amount of extracted sodium. After electrochemical oxidation, the electrode samples were taken from the cells in an inert atmosphere and tightly sealed in a sample holder equipped with a Kapton film window to avoid any side reactions in the atmosphere.

As is expected from the stepwise voltage profile of $Na_{1-x}Ni_{0.5}Mn_{0.5}O_2$, phase transition from the O3 phase to other phases is evidently confirmed by the ex situ XRD measurement for the $Na_{1-x}Ni_{0.5}Mn_{0.5}O_2$ electrode samples in Figure 5. From the XRD patterns, the characteristic diffraction

dx.doi.org/10.1021/ic300357d | Inorg. Chem. 2012, 51, 6211−6220

lines of the layered structure are observed for all $Na_{1-x}Ni_{0.5}Mn_{0.5}O_2$ samples, suggesting that the phase transition during sodium extraction occurs on the basis of $[Ni_{0.5}Mn_{0.5}]O_2$ slab gliding without breaking of Ni−O and Mn−O bonding. Lattice parameters are calculated from the diffraction patterns, and variation in the Me−Me and interslab distances is plotted in Figure 6 (the lattice parameters are found in Table S1 in the Supporting Information). In the as-prepared electrode, $x = 0$ in $Na_{1-x}Ni_{0.5}Mn_{0.5}O_2$; the pristine O3 phase is observed with nickel metal, which was used as a current collector of the sodium cells. When the sodium ions are extracted to $x = 0.1-0.2$ in $Na_{1-x}Ni_{0.5}Mn_{0.5}O_2$, the O3 phase coexists with a new layered phase, which was evident from the fact that the $(003)_{hex}$ diffraction line located at 17° (2θ) splits into two peaks. A structural analysis revealed that the new layered phase is assigned to a monoclinic O′3 phase[2a] consisting of a distorted lattice in comparison to an ideal hexagonal cell (the prime symbol refers to the monoclinic symmetry). The distortion from the hexagonal cell for these samples causes peak splitting of the Bragg diffractions, e.g., the $(104)_{hex}$ diffraction line in the O3 phase splits into $(20-2)_{mon}$ and $(111)_{mon}$ in the O′3 phase.

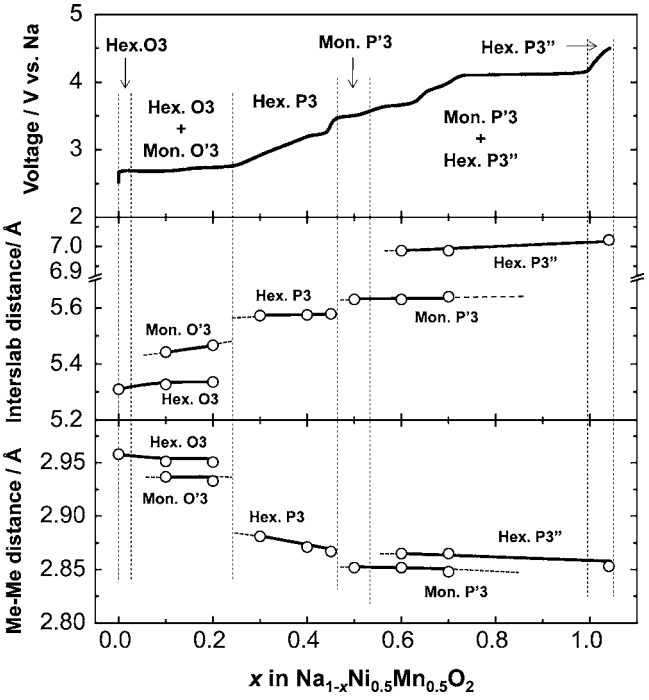

Figure 6. Change in the crystallographic parameters and phase evolution of $Na_{1-x}Ni_{0.5}Mn_{0.5}O_2$ as a function of the x value: averaged metal−metal interatomic distances (bottom) and interslab distances (middle). The first charge curve of the sodium/$NaNi_{0.5}Mn_{0.5}O_2$ cell is shown for comparison (top).

The O′3 phase disappears after subsequent removal of the sodium ions up to $x = 0.3$ in $Na_{1-x}Ni_{0.5}Mn_{0.5}O_2$. The phase transition occurs from the monoclinic O′3 phase to the hexagonal P3 phase based on the gliding mechanism of $[Mn_{0.5}Mn_{0.5}]O_2$ slabs.[2a] There is obvious evidence that the intensity of the $(104)_{hex}$ diffraction line is clearly reduced, while the $(105)_{hex}$ line becomes plainly visible.[3] In the samples of $x = 0.3$, 0.4, and 0.45 in $Na_{1-x}Ni_{0.5}Mn_{0.5}O_2$, the P3 single phase exits, and then the lattice parameters decrease with sodium removal from the lattice (Table S1 in the Supporting Information). The observation is consistent with the electrochemical behavior of the sodium cell; i.e., the operating voltage curve of the sodium cells (Figure 3) monotonously increases from $x = 0.25$ to 0.45 in $Na_{1-x}Ni_{0.5}Mn_{0.5}O_2$, suggesting that the single-phase reaction proceeds with electrochemical sodium extraction in this region.

Upon further charging to $x = 0.5$ in $Na_{1-x}Ni_{0.5}Mn_{0.5}O_2$, the diffraction lines of the P3 single phase are still observed in the pattern, and the peak profile of the P3 phase becomes asymmetrical in shape except the $(00l)$ diffraction lines, indicating a monoclinic distortion from the P3 to P′3 phase. After charging to $x = 0.6-0.7$ in $Na_{1-x}Ni_{0.5}Mn_{0.5}O_2$, in addition to the P′3 phase, new peaks appear at $2\theta = 12.7$, 25.3, and 37.2°. Analysis revealed that these peaks and all other new peaks can be assigned to the P3 phase, which has a much larger interslab distance (ca. 7.0 Å) in comparison to the P′3 phase (5.6 Å) in Figure 6. The origin of the anomalous large interslab distance will be discussed in the later section. When almost all of the sodium is extracted by charging to 4.5 V, a nearly single phase of this P3 phase is found from Figure 5. This P3 phase is denoted as the P3″ phase in Figures 5 and 6. The peak broadening is indicative of the fact that the P3″ sample has a highly faulted layer structure.

Electronic and Local Structures Observed by XAS. To investigate the valence changes of manganese and nickel, the XAS study was conducted on samples of $x = 0$ and 0.5 in

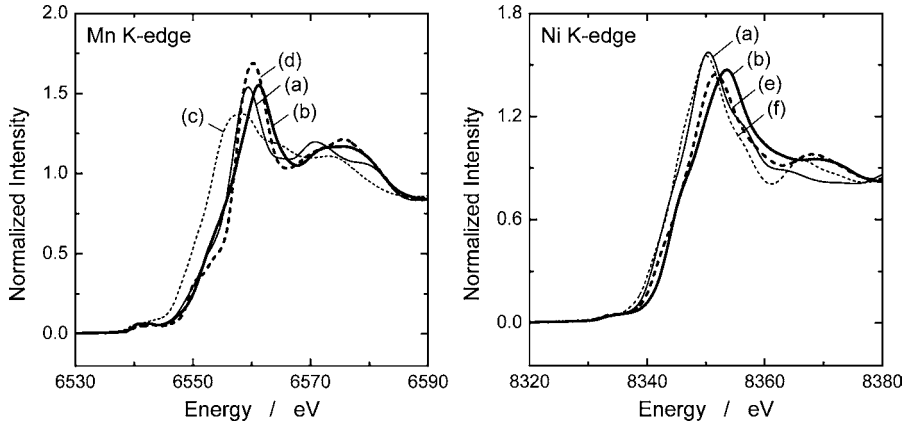

Figure 7. XANES spectra at the Mn K-edge (6539 eV) and Ni K-edge (8333 eV): (a) $NaNi_{0.5}Mn_{0.5}O_2$ and (b) $Na_{0.5}Ni_{0.5}Mn_{0.5}O_2$. XANES spectra of the reference samples are also shown: (c) Mn_2O_3, (d) Li_2MnO_3, (e) $LiNiO_2$, and (f) NiO.

dx.doi.org/10.1021/ic300357d | Inorg. Chem. 2012, 51, 6211−6220

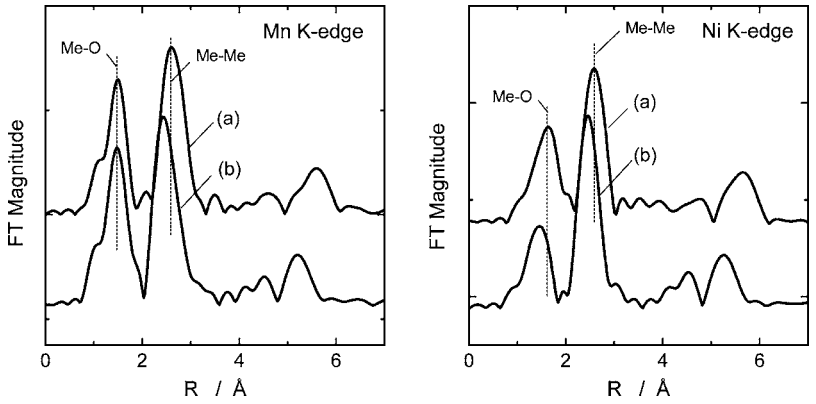

Figure 8. EXAFS spectra at the Mn and Ni K-edges: (a) $NaNi_{0.5}Mn_{0.5}O_2$ and (b) $Na_{0.5}Ni_{0.5}Mn_{0.5}O_2$. Refined structural parameters are shown in Table 2.

Table 2. Structural Parameters of $NaNi_{0.5}Mn_{0.5}O_2$ Obtained from EXAFS Measurements at the Mn and Ni K-Edges[a]

sample	shell number	S_0^2	$X-Y$ pair	CN	R (Å)	$\sigma^2(10^{-3}$ Å$^2)$	ΔE (eV)	k range	R factor (%)
$NaNi_{0.5}Mn_{0.5}O_2$	Mn1	0.71(8)	Mn−O	6	1.940(7)	5.9(9)	0.2(12)	2.0−12.7	3.0
	Mn2		Mn−(Mn, Ni)	6	2.987(2)	3.3(2)	−3.1(4)		0.9
			Mn−Na	6	3.14(1)	8.0*	−0.5(11)		
	Ni1	0.69(5)	Ni−O	6	2.068(7)	4.6(6)	−2.9(11)	2.0−12.7	3.1
	Ni2		Ni−(Mn, Ni)	6	2.969(3)	3.6(5)	−3.8(9)		5.2
			Ni−Na	6	3.17(1)	8.0*	2.5(22)		
$Na_{0.5}Ni_{0.5}Mn_{0.5}O_2$	Mn1	0.67(9)	Mn−O	6	1.926(6)	3.2(9)	1.9(15)	2.0−12.0	4.4
	Mn2		Mn−(Mn, Ni)	6	2.862(5)	2.862(5)	−8.6(15)		5.1
			Mn−Na	3	3.05*	8.0*	4.8(20)		
	Ni1	0.67(10)	Ni−O_1	4	1.920(7)	4.4(10)	−4.7(12)	2.0−12.7	4.5
			Ni−O_2	2	2.04(1)				
	Ni2		Ni−(Mn, Ni)	6	2.860(3)	3.3(4)	−5.1(10)		2.5
			Ni−Na	3	3.05*	8.0*	9.1(20)		

[a]The overall amplitude factor (S_0^2), interatomic distance (R), Debye−Waller factor (σ^2), and phase correction (ΔE) were refined. The coordination number (CN) was fixed based on the structural model.

$Na_{1-x}Ni_{0.5}Mn_{0.5}O_2$. X-ray absorption near-edge structure (XANES) spectra at Mn and Ni K-edges are shown in Figure 7. The Mn K-edge spectrum of the as-prepared $NaNi_{0.5}Mn_{0.5}O_2$ is located in a higher energy region than that of Mn_2O_3 consisting of trivalent manganese ions. In addition, because the spectrum shows a profile similar to that of $Li_2Mn^{4+}O_3$, the oxidation state of the manganese ion in $NaNi_{0.5}Mn_{0.5}O_2$ is estimated to be the tetravalent state. By a comparison of the spectra between $Na_1Ni_{0.5}Mn_{0.5}O_2$ and $Na_{0.5}Ni_{0.5}Mn_{0.5}O_2$, no significant changes are confirmed at the Mn K-edge, suggesting that manganese ions are not electrochemically active species under this condition. The slight chemical shift from $Na_1Ni_{0.5}Mn_{0.5}O_2$ to $Na_{0.5}Ni_{0.5}Mn_{0.5}O_2$ is observed in Figure 7, which is presumably due to the change in the local structure of manganese coordination. The complication of understanding the change in the XAS spectra has been discussed in the literature.[25]

In contrast to the Mn K-edge, clear changes are noted in the XANES spectra at the Ni K-edge. The Ni K-edge spectra of $NaNi_{0.5}Mn_{0.5}O_2$ and NiO closely resemble each other, suggesting that divalent nickel mainly exists at the octahedral environment in $NaNi_{0.5}Mn_{0.5}O_2$ similar to Ni^{II} surrounded with six oxide ions in NiO. The Ni K-edge absorption of $Na_{0.5}Ni_{0.5}Mn_{0.5}O_2$ clearly shifts to the higher-energy region (~2 eV) compared to that of $NaNi_{0.5}Mn_{0.5}O_2$. The spectrum is comparable in energy to that of $LiNi^{III}O_2$, suggesting that oxidation of nickel from the divalent state in $Na_1Ni_{0.5}Mn_{0.5}O_2$ to the trivalent state in $Na_{0.5}Ni_{0.5}Mn_{0.5}O_2$ occurs by electrochemical oxidation in the sodium cells. Consequently, these XAS results observed at the Mn and Ni K-edges are consistent with those of $Li_{1-x}Ni_{0.5}Mn_{0.5}O_2$,[26] even though the crystal structural transition behavior and long-range ordering of Ni−Mn are certainly different, as confirmed by ex situ XRD (Figure 5) and transmission electron microscopy (Figure S1 in the Supporting Information). It is reasonably speculated that the oxidation state of nickel changes between 2+ and 4+ for $x = 0-1$ in $Na_{1-x}Ni_{0.5}Mn_{0.5}O_2$.

EXAFS spectra at the Mn and Ni K-edges are shown in Figure 8. The refined structural parameters, obtained by EXAFS analysis, are summarized in Table 2. In the EXAFS spectra, there appear to be two intense peaks at both the Mn and Ni K-edges in the range of 1−3 Å, which are assigned to a Me−O first coordination and a Me−Me second coordination. In the first coordination shell of the as-prepared $NaNi_{0.5}Mn_{0.5}O_2$, Mn−O and Ni−O interatomic distances are calculated as 1.94 and 2.07 Å, respectively. From Shannon's ionic radii,[17] the oxidation states of the manganese and nickel ions are estimated to be in the tetravalent state (1.93 Å for Mn^{IV}−O) and the divalent state (2.09 Å for Ni^{II}−O), respectively, which are in good agreement with the interpretation of the XANES spectra. The interatomic distance of Me−O is calculated as 2.01 Å from XRD Rietveld analysis, which closely corresponds to the averaged value between Mn−O and Ni−O distances observed by EXAFS. In the second coordination shells, Mn−(Mn, Ni)

dx.doi.org/10.1021/ic300357d | Inorg. Chem. 2012, 51, 6211−6220

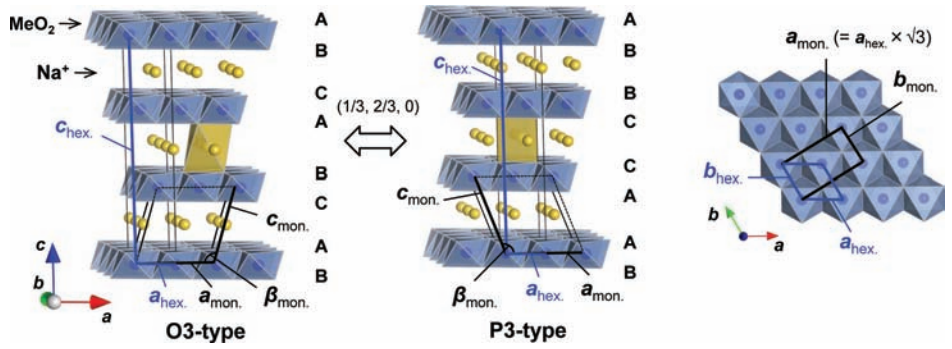

Figure 9. Schematic illustrations of the crystal structure of $Na_{1-x}Ni_{0.5}Mn_{0.5}O_2$. Sodium ions are located at the octahedral and prismatic sites in O3 and P2 types, respectively. Unit cells of hexagonal and monoclinic lattices are indicated as blue and black lines, respectively. The origin of the O′3 monoclinic phase was shifted by (−100) for comparison (left). The relationship between hexagonal and monoclinic lattices along [001] is also shown (right).

and Ni−(Mn, Ni) distances are comparable to each other, indicating that nickel and manganese ions are randomly and uniformly distributed in the transition-metal layer.

In the first coordination shell of $Na_{0.5}Ni_{0.5}Mn_{0.5}O_2$ prepared by electrochemical oxidation, almost no change is found at the Mn K-edge, while it is noted that the shortened interatomic distance and lowered Fourier transform (FT) magnitude are observed at the Ni K-edge. In this region, the nickel ions serve as electrochemically active species accompanied by sodium removal from the crystal lattice to compensate for the charge balance. As a result, the nickel ions are oxidized from the divalent to the trivalent state in $Na_{0.5}Ni_{0.5}Mn_{0.5}O_2$, whereas the manganese ions are not oxidized beyond the tetravalent state. Careful analysis by a curve-fitting procedure revealed local distortion of NiO_6 octahedra, which consists of four short Ni−O bonds (1.92 Å) and two long Ni−O bonds (2.04 Å) in Table 2. This is because of the local Jahn−Teller effect of the trivalent nickel ions ($t_{2g}^6e_g^1$ electron configuration).[27] In the second coordination shells at both the Mn and Ni K-edges, a similar shift of the decreased interatomic distances is confirmed. The Me−Me distances decrease from 2.97 to 2.86 Å after electrochemical oxidation. The change is consistent with the XRD observation; that is, the a_{hex} lattice parameters, which correspond to the in-plane interatomic distance, decrease from 2.96 Å in $Na_1Ni_{0.5}Mn_{0.5}O_2$ to 2.85 Å in $Na_{0.5}Ni_{0.5}Mn_{0.5}O_2$.

Reaction Mechanism of $Na_{1-x}Ni_{0.5}Mn_{0.5}O_2$ in the Sodium Cells. Pristine $NaNi_{0.5}Mn_{0.5}O_2$ crystallizes in the rhombohedral O3 phase. In this study, the rhombohedral unit cells are described in the hexagonal cells for simplicity. The O3 phase consists of the CCP oxygen array (ABCABC oxygen stacking shown in Figure 9). Nickel and manganese ions occupied the octahedral sites, and then (Ni, Mn)O_6 octahedra are connected by edge-sharing, forming MeO_2 slabs. Thus-formed (Ni, Mn)O_2 layers are stacked perpendicularly to (111) of the CCP lattice. Sodium ions occupy the octahedral sites, which are edge-shared sites sandwiched with (Ni, Mn)O_2 layers. $LiNi_{0.5}Mn_{0.5}O_2$ also crystallizes in the O3 phase. The interslab distance is, however, much shorter than that of $NaNi_{0.5}Mn_{0.5}O_2$; 4.75 Å for lithium[28] versus 5.32 Å for sodium.

In the early stage of the sodium extraction process ($0 < x <$ ~0.25 in $Na_{1-x}Ni_{0.5}Mn_{0.5}O_2$), the O3 phase coexists with the monoclinic O′3. The single phase of the O′3 phase might be obtained at x = ~0.25. The structural relationship between the O3 and O′3 phases is also shown in Figure 9. The general affine transformation of the coordinate system from the hexagonal O3 phase to the monoclinic O′3 phase (space group $C2/m$) is given by the following relationship:[29]

$$(a_{mon}, b_{mon}, c_{mon}) = (a_{hex}, b_{hex}, c_{hex})\begin{pmatrix} -2 & 0 & \frac{2}{3} \\ -1 & -1 & \frac{1}{3} \\ 0 & 0 & \frac{1}{3} \end{pmatrix} \quad (1)$$

From the lattice parameter of the O′3 phase at x = 0.1 and 0.2 (Table S1 in the Supporting Information), the value of $a_{mon}/\sqrt{3}$ = 2.89 Å, which is ca. 1.5% larger than that of b_{mon} = 2.94 Å, indicating distortion of the in-plane metal arrangements within the slabs. The β angle of the monoclinic cell is calculated as ca. 110°, which clearly deviates from the 108° in the ideal hexagonal cell observed in $NaNi_{0.5}Mn_{0.5}O_2$. Such a distortion from the ideal rhombohedra lattice results in peak splitting of the Bragg diffraction lines shown in Figure 5.

The phase transition from the O′3 to P3 phase was induced by the further sodium extraction process (x = ~0.3). The single-phase reaction proceeds as the P3 phase in the range of $0.3 < x < 0.45$. The space group symmetry of the P3 phase is the same as that of the O3 phase, which is the rhombohedral $R\bar{3}m$. Part of the MeO_2 slabs glides by ($^1/_3$, $^2/_3$, 0),[2a,3] resulting in formation of the P3 phase. In the P3 phase, the (x, y) coordinates of the oxygen atoms are the same between the interslab space, forming prismatic sodium sites (ABBCCA oxygen stacking in Figure 9). The prismatic sites are connected by both edge and face sharing with MeO_6 octahedra in the slabs. Generally, the observed structural transition behavior in $Na_{1-x}Ni_{0.5}Mn_{0.5}O_2$ (between O3 and P3) is similar to that of previous reports for the sodium layered oxides such as Na_xCoO_2[2a−c] and $Na_xNi_{0.6}Co_{0.4}O_2$.[3] The structural transition is contrary to the lithium system of $Li_{1-x}Ni_{0.5}Mn_{0.5}O_2$, in which a single phase of the O3 phase is generally observed.

The P3 phase further changes into the monoclinic P′3 phase. It has been confirmed that the crystal structure of $Na_{0.5}Ni_{0.5}Mn_{0.5}O_2$ is assigned to be the monoclinic P′3-type phase (space group $C2/m$). Transformation from the P3 to P′3 phase is formulated by the following relationship:[30]

dx.doi.org/10.1021/ic300357d | Inorg. Chem. 2012, 51, 6211−6220

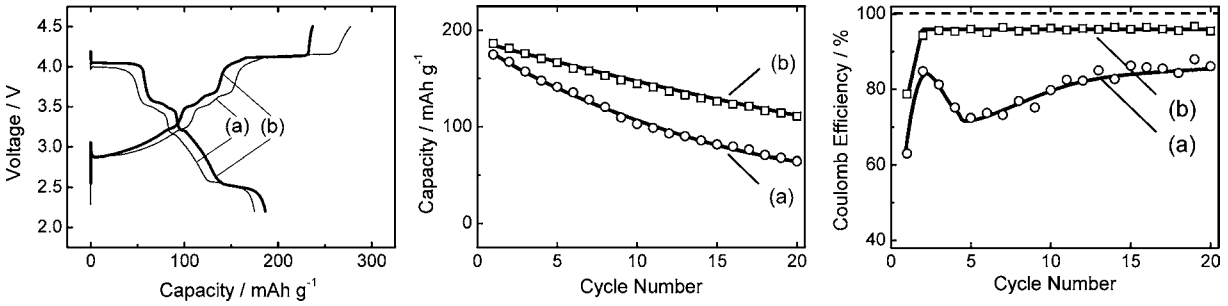

Figure 10. (left) Initial galvanostatic charge/discharge curves of the sodium/$NaNi_{0.5}Mn_{0.5}O_2$ coin-type cells at a rate of 1/10 C (24 mA g^{-1}) in the voltage range of 2.2−4.5 V in 1 M $NaClO_4$ dissolved in PC: (a) FEC-free and (b) with 2 vol % FEC. The discharge capacity retention (center) and Coulombic efficiency (right) of the sodium/$NaNi_{0.5}Mn_{0.5}O_2$ cells are also shown.

$$(a_{mon}, b_{mon}, c_{mon}) = (a_{hes}, b_{hex}, c_{hex})\begin{pmatrix} 1 & 1 & -\frac{1}{3} \\ -1 & 1 & \frac{1}{3} \\ 0 & 0 & \frac{1}{3} \end{pmatrix} \quad (2)$$

In P′3-type $Na_{0.5}Ni_{0.5}Mn_{0.5}O_2$, in-plane distortion estimated from the ratio between $a_{mon}/\sqrt{3}$ and b_{mon} is ca. 0.5%, which is less distortion than that of the O′3 phase. In fact, clear peak separation of the Bragg diffraction lines was not observed in the XRD pattern. It is also consistent with the observation by EXAFS spectra that the intensity of the FT magnitude in the second coordination shell is only slightly influenced by sodium extraction to x = ∼0.5 (Figure 8).

Another structural transition occurs by further extraction of the sodium ions from P′3-type $Na_{0.5}Ni_{0.5}Mn_{0.5}O_2$. The P′3-type phase coexists with the P3″ phase, which has a much larger interslab distance (ca. 7.0 Å) in comparison to the P3 phase observed in 0.3 < x < 0.45 (ca. 5.55 Å). Because the interslab distance of the P3″ phase is as anomalously large as the sodium metal oxides reported so far, it has been speculated that electrolyte solvent molecules and/or salt ions were inserted between the slabs. Such an intercalation of the molecules has been reported in P2-type $Na_{2/3}[Co_{1/3}Mn_{2/3}]O_2$.[31] Water molecules are intercalated in the sample by exposure to humid air, forming $Na_{2/3}(H_2O)_{2/3}[Co_{1/3}Mn_{2/3}]O_2$. The interslab space became larger from 5.65 Å for the as-prepared $Na_{2/3}[Co_{1/3}Mn_{2/3}]O_2$ to 7.05 Å for $Na_{2/3}(H_2O)_{2/3}$-$[Co_{1/3}Mn_{2/3}]O_2$. The interslab distance is very similar to that of our observed P3″ phase in x > 0.5 in $Na_{1-x}Ni_{0.5}Mn_{0.5}O_2$ after charging to 4.5 V. Although a detailed explanation was not provided, a similar anomalous interlayer distance (∼7.0 Å) was also reported at x = 0.73 in Na_xMnO_2.[32] In contrast to the sodium system, the interslab distance of $Li_{0.2}Ni_{0.5}Mn_{0.5}O_2$ still remains as less than 4.8 Å,[28] which may not be able to allow molecule intercalation between the narrower interslab space. Further systematic study is needed to test this hypothesis. In Figure 3, there appear to be several one- and two-phase domains in the charge curve from x = 0.5 to 1.0 in $Na_{1-x}Ni_{0.5}Mn_{0.5}O_2$ showing complicated phase transitions including the P′3 and P3″ phases. To prove the exact phase transition and Na^+/vacancy ordering, more precise measurement coupled with an in situ XRD experiment are required, as was recently reported by Delmas' group.[2c]

As was already described in Figure 3, the phase transition is reversible during sodium deintercalation and intercalation. Electrochemical reversibility as the sodium insertion materials for rechargeable batteries is expected to deteriorate by intercalation of the molecule. Nevertheless, the large reversible capacity of 185 mAh g^{-1} was still observed after charging to 4.5 V (Figure 3). The poor cycleability in this wide voltage range (Figure 4d), however, might originate from the anomalously extended interslab space and/or the molecule intercalation observed by ex situ XRD. In fact, $Li_xNi_{0.5}Mn_{0.5}O_2$ shows a much better cycling ability even in the higher potential range (∼5.0 V vs lithium).[28] The cycleability of $Na_{1-x}Ni_{0.5}Mn_{0.5}O_2$ is significantly improved by lowering of the cutoff voltage to 3.8 V (Figure 4), even though structural transitions from the O3 to P′3 phase are unavoidable. From these results, it is expected that the cycleability and reversible capacity of $Na_{1-x}Ni_{0.5}Mn_{0.5}O_2$ as positive electrode materials for sodium-ion batteries are further improved by the proper selection of the electrolyte solution, which can suppress intercalation of the molecules between the slabs upon high-voltage exposure.

To test this hypothesis, we have examined electrolyte additives and found that FEC highly improves the reversibility of $Na_{1-x}Ni_{0.5}Mn_{0.5}O_2$ as the electrolyte additive.[23] Figure 10 shows charge/discharge curves of the sodium/$NaNi_{0.5}Mn_{0.5}O_2$ cells in the voltage range of 2.0−4.5 V in 1 mol dm^{-3} $NaClO_4$/PC with 2 vol % FEC as the electrolyte additive. Conventional coin-type cells were used in these tests. The detailed experimental setup can be found in our recent literature.[23] Polarization of the discharge process is effectively reduced by the addition of FEC in PC. The initial Coulombic efficiency is also improved from 63 to 79% under this condition. In successive cycles, the efficiency is greatly improved from about 80% to >95% by FEC addition. We have already reported that suppression of the oxidation of the electrolyte decomposition products, which were produced at the sodium metal electrode surface, is responsible for improving the Coulombic efficiency.[23] In addition, the cycleability of the sodium cells is remarkably improved by the addition of the electrolyte additive, as shown in Figure 10. Although the reversibility is slightly increased compared with the beaker-type cell in Figure 4d, the discharge capacity declines rapidly below 65 mAh g^{-1} for the FEC-free PC after 20 cycles. The discharge capacity at the 20th cycle is increased to 110 mAh g^{-1} under the same condition with 2 vol % FEC. From these results, it is concluded that the electrolyte selection is the important factor to further improve the electrode performance of the sodium insertion materials in the future.

dx.doi.org/10.1021/ic300357d | Inorg. Chem. 2012, 51, 6211−6220

CONCLUSIONS

In conclusion, electrochemically reversible sodium extraction and insertion into/from $Na_{1-x}Ni_{0.5}Mn_{0.5}O_2$ has been demonstrated at room temperature. The sodium/$NaNi_{0.5}Mn_{0.5}O_2$ cells can deliver more than 185 mAh g^{-1} of reversible capacity after full sodium extraction. The electrode reversibility is significantly influenced by the charging condition and electrolyte additives, such as FEC. When the sodium/$NaNi_{0.5}Mn_{0.5}O_2$ cells are cycled in the voltage domain between 2.2 and 3.8 V, $NaNi_{0.5}Mn_{0.5}O_2$ demonstrates 125 mAh g^{-1} with acceptable capacity retention over the 50 continuous cycling tests at the C/5 rate (48 mA g^{-1}). The cycleability and Coulombic efficiency are further improved by the addition of FEC. The XAS study shows that charge compensation during sodium extraction/insertion is mainly achieved by the nickel ion based on Ni^{2+}/Ni^{4+} redox via Ni^{3+}. Manganese ions are found to be electrochemically inactive species. Structural evolution during the sodium extraction process from $NaNi_{0.5}Mn_{0.5}O_2$ is examined by the ex situ XRD method; the O3 phase in the as-prepared $NaNi_{0.5}Mn_{0.5}O_2$ continuously changes to the O′3, P3, P′3, and then P3″ phase upon charging. The P3″ phase is assumed to incorporate the solvent molecules in the interstitial space between the $[Ni_{0.5}Mn_{0.5}]O_2$ slabs because the anomalously large interslab distances (~7.0 Å) such as the layered oxides are observed. In this paper, we have demonstrated that $NaNi_{0.5}Mn_{0.5}O_2$ is a robust and durable positive electrode material, suggesting that the material will be one of a promising candidate as a positive electrode material for rechargeable sodium-ion batteries.

ASSOCIATED CONTENT

Supporting Information

Lattice parameters and images of the $NaNi_{0.5}Mn_{0.5}O_2$ single particle. This material is available free of charge via the Internet at http://pubs.acs.org.

AUTHOR INFORMATION

Corresponding Author

*E-mail: komaba@rs.kagu.tus.ac.jp. Tel./Fax: +81-3-5228-8749.

Notes

The authors declare no competing financial interest.

ACKNOWLEDGMENTS

This study was, in part, granted by the Japan Society for the Promotion of Science through the "Funding for NEXT Program", initiated by the Council for Science and Technology Policy and by KAKENHI (Grant 21750194).

REFERENCES

(1) Abraham, K. M. *Solid State Ionics* **1982**, *7* (3), 199–212.
(2) (a) Delmas, C.; Braconnier, J. J.; Fouassier, C.; Hagenmuller, P. *Solid State Ionics* **1981**, *3–4* (Aug), 165–169. (b) Shacklette, L. W.; Jow, T. R.; Townsend, L. *J. Electrochem. Soc.* **1988**, *135* (11), 2669–2674. (c) Berthelot, R.; Carlier, D.; Delmas, C. *Nat. Mater.* **2011**, *10* (1), 74–80. (d) Carlier, D.; Blangero, M.; Ménétrier, M.; Pollet, M. l.; Doumerc, J.-P.; Delmas, C. *Inorg. Chem.* **2009**, *48* (15), 7018–7025.
(3) Saadoune, I.; Maazaz, A.; Menetrier, M.; Delmas, C. *J. Solid State Chem.* **1996**, *122* (1), 111–117.
(4) (a) Doeff, M. M.; Peng, M. Y.; Ma, Y. P.; Dejonghe, L. C. *J. Electrochem. Soc.* **1994**, *141* (11), L145–L147. (b) Ma, X.; Chen, H.; Ceder, G. *J. Electrochem. Soc.* **2011**, *158* (12), A1307–A1312.
(5) Okada, S.; Yamaki, J. Iron-Based Rare-Metal-Free Cathodes. In *Lithium Ion Rechargeable Battries*; Ozawa, K., Ed.; Wiley-VCH: Weinheim, Germany, 2009; p 57.
(6) Takeda, Y.; Nakahara, K.; Nishijima, M.; Imanishi, N.; Yamamoto, O.; Takano, M.; Kanno, R. *Mater. Res. Bull.* **1994**, *29* (6), 659–666.
(7) Whittingham, M. S. *J. Electrochem. Soc.* **1975**, *122* (5), 713–714.
(8) (a) Komaba, S.; Mikumo, T.; Ogata, A. *Electrochem. Commun.* **2008**, *10* (9), 1276–1279. (b) Komaba, S.; Mikumo, T.; Yabuuchi, N.; Ogata, A.; Yoshida, H.; Yamada, Y. *J. Electrochem. Soc.* **2010**, *157* (1), A60–A65.
(9) Nishijima, M.; Gocheva, I. D.; Okada, S.; Doi, T.; Yamaki, J.; Nishida, T. *J. Power Sources* **2009**, *190* (2), 558–562.
(10) (a) Shiratsuchi, T.; Okada, S.; Yamaki, J.; Nishida, T. *J. Power Sources* **2006**, *159* (1), 268–271. (b) Trad, K.; Carlier, D.; Croguennec, L.; Wattiaux, M.; Lajmi, B.; Ben Amara, M.; Delmas, C. *J. Phys. Chem. C* **2010**, *114* (21), 10034–10044. (c) Lee, K. T.; Ramesh, T. N.; Nan, F.; Botton, G.; Nazar, L. F. *Chem. Mater.* **2011**, *23* (16), 3593–3600.
(11) (a) Recham, N.; Chotard, J.-N.; Dupont, L.; Djellab, K.; Armand, M.; Tarascon, J.-M. *J. Electrochem. Soc.* **2009**, *156* (12), A993–A999. (b) Kawabe, Y.; Yabuuchi, N.; Kajiyama, M.; Fukuhara, N.; Inamasu, T.; Okuyama, R.; Nakai, I.; Komaba, S. *Electrochem. Commun.* **2011**, *13* (11), 1225–1228. (c) Ellis, B. L.; Makahnouk, W. R. M.; Makimura, Y.; Toghill, K.; Nazar, L. F. *Nat. Mater.* **2007**, *6* (10), 749–753.
(12) Lu, Z.; Dahn, J. R. *J. Electrochem. Soc.* **2001**, *148* (11), A1225–A1229.
(13) Delmas, C.; Fouassier, C.; Hagenmuller, P. *Physica B & C* **1980**, *99* (1–4), 81–85.
(14) Kim, D.; Kang, S.-H.; Slater, M.; Rood, S.; Vaughey, J. T.; Karan, N.; Balasubramanian, M.; Johnson, C. S. *Adv. Energy Mater.* **2011**, *1* (3), 333–336.
(15) (a) Komaba, S.; Takei, C.; Nakayama, T.; Ogata, A.; Yabuuchi, N. *Electrochem. Commun.* **2010**, *12* (3), 355–358. (b) Komaba, S.; Nakayama, T.; Ogata, A.; Shimizu, T.; Takei, C.; Takada, S.; Hokura, A.; Nakai, I. *ECS Trans.* **2009**, *16* (42), 43–55. (c) Komaba, S.; Murata, W.; Ishikawwa, T.; Yabuuchi, N.; Ozeki, T.; Nakayama, T.; Ogata, A.; Gotoh, K.; Fujiwara, K. *Adv. Funct. Mater.* **2011**, *21* (20), 3859–3867.
(16) (a) Ohzuku, T.; Makimura, Y. *Chem. Lett.* **2001**, *30* (8), 744–745. (b) Makimura, Y.; Ohzuku, T. *J. Power Sources* **2003**, *119*, 156–160.
(17) Shannon, R. D. *Acta Crystallogr., Sect. A* **1976**, *32* (SEP1), 751–767.
(18) (a) Paulsen, J. M.; Dahn, J. R. *J. Electrochem. Soc.* **2000**, *147* (7), 2478–2485. (b) Kang, K. S.; Meng, Y. S.; Breger, J.; Grey, C. P.; Ceder, G. *Science* **2006**, *311* (5763), 977–980.
(19) Izumi, F.; Ikeda, T. A Rietveld-analysis program RIETAN-98 and its applications to zeolites. In *European Powder Diffraction*; Delhez, R., Mittemeijer, E. J., Eds.; Trans Tech Publications Ltd.: Zurich, Switzerland, 2000; Vols. *321–323*, Parts 1 and 2, pp 198–203.
(20) Newville, M. *J. Synchrotron Radiat.* **2001**, *8*, 322–324.
(21) Rehr, J. J.; Albers, R. C. *Rev. Mod. Phys.* **2000**, *72* (3), 621–654.
(22) (a) Meng, Y. S.; Ceder, G.; Grey, C. P.; Yoon, W. S.; Jiang, M.; Breger, J.; Shao-Horn, Y. *Chem. Mater.* **2005**, *17* (9), 2386–2394. (b) Yabuuchi, N.; Lu, Y.-C.; Mansour, A. N.; Chen, S.; Shao-Horn, Y. *J. Electrochem. Soc.* **2011**, *158* (2), A192–A200.
(23) Komaba, S.; Ishikawa, T.; Yabuuchi, N.; Murata, W.; Ito, A.; Ohsawa, Y. *ACS Appl. Mater. Interfaces* **2011**, *3* (11), 4165–4168.
(24) Ong, S. P.; Chevrier, V. L.; Hautier, G.; Jain, A.; Moore, C.; Kim, S.; Ma, X. H.; Ceder, G. *Energy Environ. Sci.* **2011**, *4* (9), 3680–3688.
(25) Yabuuchi, N.; Yoshii, K.; Myung, S.-T.; Nakai, I.; Komaba, S. *J. Am. Chem. Soc.* **2011**, *133* (12), 4404–4419.
(26) Yoon, W. S.; Paik, Y.; Yang, X. Q.; Balasubramanian, M.; McBreen, J.; Grey, C. P. *Electrochem. Solid State Lett.* **2002**, *5* (11), A263–A266.

(27) Rougier, A.; Delmas, C.; Chadwick, A. V. *Solid State Commun.* **1995**, *94* (2), 123−127.
(28) Yabuuchi, N.; Kumar, S.; Li, H. H.; Kim, Y. T.; Shao-Horn, Y. *J. Electrochem. Soc.* **2007**, *154* (6), A566−A578.
(29) Shao-Horn, Y.; Levasseur, S.; Weill, F.; Delmas, C. *J. Electrochem. Soc.* **2003**, *150* (3), A366−A373.
(30) Blangero, M.; Carlier, D.; Pollet, M.; Darriet, J.; Delmas, C.; Doumerc, J. P. *Phys. Rev. B* **2008**, *77* (18), 184116-1−184116-8.
(31) Lu, Z. H.; Dahn, J. R. *Chem. Mater.* **2001**, *13* (4), 1252−1257.
(32) Mendiboure, A.; Delmas, C.; Hagenmuller, P. *J. Solid State Chem.* **1985**, *57* (3), 323−331.